



1 **Drought reconstruction since 1796 CE based on tree-ring widths in the Upper**
2 **Heilongjiang (Amur) River Basin in Northeast Asia, and its linkage to Pacific**
3 **Ocean climate variability**

4 Yang Xu ¹, Heli Zhang ², Feng Chen ^{1*}, Shijie Wang ¹, Mao Hu ¹, Martín Hadad ³, Fidel Roig ^{4,5}
5 *1. Yunnan Key Laboratory of International Rivers and Transboundary Eco-Security, Institute of*
6 *International Rivers and Eco-Security, Yunnan University, Kunming 650500, China*
7 *2. Key Laboratory of Tree-ring Physical and Chemical Research of China Meteorological*
8 *Administration/ Xinjiang Key Laboratory of Tree-ring Ecology, Institute of Desert Meteorology,*
9 *China Meteorological Administration, Urumqi 830002, China*
10 *3. Laboratorio de Dendrocronología de Zonas Áridas. CIGEOBIO (CONICET-UNSJ), San Juan,*
11 *Argentina, Gabinete de Geología Ambiental (INGEO-UNSJ), Av. Ignacio de la Roza 590 (oeste),*
12 *J5402DCS Rivadavia, San Juan, Argentina*
13 *4. Laboratorio de Dendrocronología e Historia Ambiental, IANIGLA-CCT CONICET, Mendoza,*
14 *Argentina*
15 *5. Hémera Centro de Observación de la Tierra, Escuela de Ingeniería Forestal, Facultad de*
16 *Ciencias, Universidad Mayor, Camino La Pirámide 5750, Huechuraba, Santiago 8580745, Chile*
17 *Correspondence: feng653@163.com

18 **Abstract:** The economic and environmental impacts of persistent droughts in East
19 Asia are of growing concern, and therefore it is important to study the cyclicality and
20 causes of these regional droughts. The self-calibrating Palmer Drought Severity Index
21 (scPDSI) has been extensively employed to describe the severity of regional drought,
22 and several PDSI reconstructions based on tree rings have been produced. We
23 compiled a tree-ring chronology for Hailar pine (*Pinus sylvestris* var. *Mongolica*)
24 from two sites in the Hailar region in the Upper Heilongjiang (Amur) River Basin.
25 Analysis of the climate response revealed that scPDSI was the primary factor limiting



26 tree ring growth from May to July. The mean May to July scPDSI in the Hailar region
27 since 1796 was reconstructed from the tree-ring width chronology. The results of
28 spatial correlation analysis revealed that the reconstructed scPDSI in this region
29 responded significantly to climate change. Analysis of the synoptic climatology
30 indicated that the drought in the Upper Heilongjiang (Amur) River Basin is closely
31 related to ENSO and the Silk Road teleconnection. The results of atmospheric water
32 cycle analysis show that water vapor transport processes are the dominant factor in
33 the development of drought in this region.

34 **Keywords:** Tree rings; ScPDSI reconstruction; Sea surface temperature;
35 **Severe drought; Moisture recycling**

36 **1. Introduction**

37 Drought—accompanied by persistent high temperatures and below-average
38 precipitation over intervals of months to years—is of growing concern. As a natural
39 disaster, the frequency and duration of drought have increased as global warming has
40 intensified. The impact of drought on human well-being and economic productivity is
41 also increasing, given that drought severely threatens food and water security (Lesk et
42 al. 2016; Trenberth et al. 2014; Wang et al. 2016; Chen et al. 2022). Due to regional
43 water shortages, droughts frequently wreak havoc on agriculture and the quality of
44 life in northeast China (NEC). Hence, understanding the variability of drought in this
45 region and its causal mechanisms is essential for both drought prediction and the
46 formulation of disaster response strategies (Li et al. 2019; Yuan and Wood 2013).

47 However, only short-duration instrumental records of drought variability are



48 available for NEC, most of them from the 1950s onwards. However, this deficiency
49 can be addressed via proxy paleoclimate records, such as tree-ring widths (Fritts,
50 1991). With their high annual precision and extensive coverage, tree rings have been
51 used as a reliable proxy for reconstructing historical climatic and hydrological
52 changes (Cook et al. 2016; Chen et al. 2021; Pearson et al. 2020). Hailar is located in
53 the Upper Heilongjiang (Amur) River Basin, in the woodland-steppe interface of NEC,
54 part of the eastern edge of the Hulunbuir grasslands, a region highly susceptible to
55 climatic and environmental changes and that has experienced drought over the past
56 few decades (Zhang et al. 1997; Wang et al. 2010; Bao et al. 2015; Chen et al. 2012).
57 Drought reconstructions based on tree-ring widths can potentially make a valuable
58 contribution to regional planning and ecological conservation in this region. Over the
59 past two decades, several studies based on tree-ring width have been conducted in
60 Northeast Asia (Cook et al. 2010; Liang et al. 2007; Bao et al. 2015; Chen et al. 2012;
61 Liu et al. 2016; Liu et al. 2009). However, research attention needs to be directed to
62 the agro-pastoral zone in the western part of NEC, where the fragile ecology and
63 climate sensitivity necessitate a greater understanding of the patterns and mechanisms
64 of drought.

65 Severe drought events are a serious problem in northern China, especially since the
66 late 1970s, when the weakening of the East Asian Summer Monsoon (EASM)
67 contributed to the 'southern flooding and northern drought' climatic pattern, with
68 frequent intense drought events in the north (Wang, 2002; Yu et al. 2004; Ding et al.
69 2009). Regarding the climatic mechanisms responsible for the NEC drought, it has



70 been suggested that variations in the Pacific Ocean interdecadal oscillation (PDO) and
71 in Arctic Ocean sea-ice cover have contributed to an interdecadal decrease in
72 precipitation in NEC, leading to drought (Han et al. 2015). It has also been suggested
73 that the global distribution of sea surface temperature and ENSO events are closely
74 linked to summer precipitation in NEC, thus explaining the summer drought
75 mechanism in the NEC from an interannual perspective (Han et al. 2017). Winter
76 NAO has also been shown to impact the interannual variability of summer drought
77 events in NEC (Fu and Zeng, 2005). Anticyclonic circulation anomalies can often
78 trigger extreme and prolonged drought events. Such anomalies always occur as a
79 major product of specific remote teleconnection patterns, called stationary wave
80 patterns (Schubert et al. 2014). Several steady wave models have been shown to
81 generate extreme drought events, with the 2014 summer drought in northern China
82 attributed to the EU pattern. It has also been confirmed that the Silk Road,
83 Pacific-Japanese, and EU models caused the July–August 2014 drought in north and
84 northeastern China (Wang and He, 2015; Wang et al. 2017; Xu et al. 2017). While
85 many of the above studies describe water vapor flux anomalies during periods of
86 extreme drought, our understanding of the role of water vapor derived from local
87 evaporation and advective transport is limited. Quantifying the contribution of
88 advected water vapor transport and precipitation circulation processes to precipitation
89 is essential for understanding the water vapor cycle and anticipating the intensity of
90 severe drought episodes (Findell and Eltahir, 2003; Guan et al. 2022).

91 The objectives of the present study are: (1) To reconstruct the scPDSI of the Hailar



92 region and to analyze changes in the temporal variations of regional drought; (2) to
93 determine the atmospheric circulation mechanisms generating extreme drought events;
94 and (3) to analyze the contribution of advective water vapor transport and local
95 evaporation to precipitation during droughts, and to determine their leading causes.

96 **2. Materials and Methods**

97 **2.1 Study area**

98 Tree-ring sampling sites NEG1 (119°36' E, 47°58' N, 600-700m a.s.l.) and MGET
99 (119°24' E, 47°59' N, 1100-1200 m a.s.l.) are located in the Upper Heilongjiang
100 (Amur) River Basin (Fig. 1). The region lies within the arid and semi-arid region of
101 NEC, on the eastern edge of the Hulunbeier steppe and close to the western slopes of
102 the Greater Khingan Range. This region has a continental and monsoonal climate.
103 Due to the incursion of high-latitude cold and dry air masses in winter and of warm
104 and moist air masses from low-latitude areas in summer, the climate tends to alternate
105 between cold and dry in winter and warm and humid in summer. The average annual
106 temperature is around -0.9 °C and the average yearly precipitation is ~382.8 mm (Fig.
107 2a). December–January is the coldest period, with sparse rainfall, while June–August
108 is the hottest period when precipitation is abundant (Fig. 2b). Thus, the climate is
109 generally cold and dry. The grassland in this region is undergoing severe
110 desertification and degradation in response to global and regional climate change
111 (Zhang et al. 2011).

112 **2.2 Tree-ring data**

113 The dominant tree species in the Hailar region is Hailar pine (*Pinus sylvestris* var.



114 *Mongolica*), which was sampled for tree-ring analysis. Both sites were located at the
115 upper tree line, on steep slopes with thin soils. Information about the sampling sites is
116 given in Table 1. Samples were taken from chest height using a 10-mm diameter
117 incremental borer. Forty cores were collected from 20 trees at sampling site NEGC,
118 and 63 cores were collected from 33 trees at sampling site MGET. In the laboratory,
119 the core samples were dried, mounted and successively sanded with 320- and 600-grit
120 sandpaper until the tree-ring widths were visible, and were then imaged using a
121 high-precision scanner. Tree-ring width data were measured using CooRecorder 9.4
122 software, and the data quality was checked by cross-matching using the quality
123 control program COFFCHA (Holmes, 1983). The ARSTAN procedure was then used
124 to remove non-climatic influences on the tree-ring width data, due to age and growth,
125 using exponential detrending. This procedure resulted in a standardized
126 chronology of tree-ring widths (STD), a chronology of differences (RES), and an
127 autoregressive chronology (ARS). The individual detrended chronologies from the
128 two sites were combined to produce a new RC chronology using a robust averaging
129 method (Cook, 1985). The STD chronology was selected to retain high and
130 low-frequency variations based on the considerations of subsequent analyses. The
131 data series were truncated according to thresholds of at least $EPS > 0.85$ and 6 (3 trees)
132 for the expressed population signal and sample size, respectively, resulting in a
133 reliable reconstruction for the period of 1796–2020.

134 **2.3 Climate data and statistical methods**

135 Monthly instrumental climate data from Hailar meteorological station (49°15' E,



136 119°42' N, 650 m a.s.l.), affiliated to the National Meteorological Administration of
137 China, including monthly mean temperature and monthly total precipitation, were
138 obtained for the period of 1951–2020. Monthly mean runoff data from Khabarovsk
139 Hydrological Station on the lower Heilongjiang River were used to analyze the
140 response of the reconstructed scPDSI to runoff variations. The locations of the
141 meteorological and hydrological stations are shown in Fig. 2a. scPDSI gridded
142 climate data of CRU TS 4.06 from the Climate Research Unit (CRU) of the
143 University of East Anglia were also used in this study (Harris et al. 2014). SPSS 22.0
144 was used to assess the correlation of the climate signals contained in the three
145 chronologies for the individual months from July of the previous year to September of
146 the current year. Based on the results of this correlation analysis, several seasonal
147 climate combinations from July of the last year to September of the current year were
148 filtered, and the seasonal climate combinations with the highest correlation were
149 selected for climate reconstruction, using one-dimensional linear regression. A split
150 calibration-verification test was used to test the reliability of the reconstructed models,
151 dividing the period of 1951–2020 into independent calibration and validation periods.
152 The main parameters assessed were the correlation coefficient (R), explained variance
153 (R^2), efficiency coefficient (CE), error reduction value (RE), sign test ($ST1$), and the
154 first-order difference sign test ($ST2$) (Cook and Kairiukstis, 2013). In this study, after
155 15-year low-pass filtering, intervals of more than 10 years below/above the mean of
156 the reconstructed series were defined as dry/wet periods, and the years below or
157 above 1.5 times the standard deviation of the series mean were defined as extreme



158 dry/wet years. The quasi-periodic characteristics of the reconstructed scPDSI were
159 analyzed using Multitaper spectral analysis (MTM) (Mann and Lees, 1996). Spatial
160 correlation maps were generated between the reconstructed scPDSI series and the grid
161 data, including precipitation and scPDSI data from CRU TS 4.06, and runoff grid
162 point data from G-RUN (Harris et al. 2014; Ghiggi et al. 2021).

163 **2.4 Land-atmosphere water balance**

164 The Brubaker binary model has been used to quantify the contribution of external
165 water vapor transport and local evaporative water vapor to precipitation, based on the
166 atmospheric water vapor balance (Brubaker et al. 1993). The water vapor equation for
167 the vertical integration per unit area can be expressed as follows (Brubaker et al. 1993;
168 Guo et al. 2018):

$$\frac{\partial Q}{\partial t} = - \left(\frac{\partial F_u}{\partial x} + \frac{\partial F_v}{\partial y} \right) + E - P, \quad (1)$$

169 Where Q is the vertically integrated water vapor concentration; F_u and F_v are the
170 vertically integrated latitudinal and meridional water vapor fluxes, respectively; and
171 E and P are the vertically integrated land evaporation and rainfall, respectively.

172 Compared to the magnitude of the water vapor flux, the vertically integrated water
173 vapor content varies very little over time and is insignificant on longer timescales
174 (Burde and Zangvil, 2001). Thus, if the left side of equation (1) is 0, we obtain the
175 following equation:

$$\left(\frac{\partial F_u}{\partial x} + \frac{\partial F_v}{\partial y} \right) = E - P, \quad (2)$$

176 Assuming that externally imported water vapor and locally evaporated water vapor
177 are well mixed over the study area, and that the proportions of evaporated and



178 advected water vapor contribute equally to the development of precipitation and
179 moisture fluxes, the proportional relationship can be obtained, as follows (Zhao and
180 Zhou, 2021; Guo et al. 2018; Li et al. 2020):

$$\frac{P_a}{P} = \frac{Q_a}{Q}, \quad (3)$$

$$\frac{P_e}{P} = \frac{Q_e}{Q}, \quad (4)$$

181 Where Q_a and Q_e represent the water vapour content resulting from external
182 water vapour transport and local land surface evaporation, respectively, and P_e and
183 P_a are the precipitation amounts resulting from evaporation and the external transport
184 of water vapor, respectively. In addition, the water vapor balance equation for the
185 external water vapor transport term is as follows (Guo et al. 2018; Zhao and Zhou,
186 2021; Li et al. 2020):

$$-\left(\frac{\partial F_u^a}{\partial x} + \frac{\partial F_v^a}{\partial y}\right) = P_a \quad (5)$$

187 Where F_u^a and F_v^a represent the vertically integrated latitudinal and longitudinal
188 water vapor transport from external inputs, respectively, assuming P , E and P_a are
189 constant within the study area during the interval of concern (Burde and Zangvil,
190 2001). Using the above assumptions and the Gaussian scattering assumptions,
191 equations (2) and (5) can be applied to a region of area A (in m), as follows:

$$-\left(\frac{\partial F_u}{\partial x} + \frac{\partial F_v}{\partial y}\right) |A = F_{in} - F_{out} = (P - E)A \quad (6)$$

$$-\left(\frac{\partial F_u^a}{\partial x} + \frac{\partial F_v^a}{\partial y}\right) |A = F_{in} - F_{out-a} = P_a A \quad (7)$$

192 Here, $-\left(\frac{\partial F_u}{\partial x} + \frac{\partial F_v}{\partial y}\right) |A$ and $-\left(\frac{\partial F_u^a}{\partial x} + \frac{\partial F_v^a}{\partial y}\right) |A$ represent the total water vapour
193 irradiation dispersion in the targeted region and the irradiation dispersion of externally
194 transported water vapor, respectively; F_{out} and F_{out-a} represent the total water



195 vapour leaving the calculated area and the part of the external input water vapour
196 flowing away from the calculated area again, respectively; and F_{in} represents the
197 total water vapor transported to the targeted area from outside. This enables an
198 estimate to be made of the contribution of external moisture transport and local land
199 surface evaporation to precipitation, as follows (Guo et al. 2018; Li et al. 2020):

$$r = \frac{P_a}{P} = \frac{2F_{in}}{2F_{in} + EA} \quad (8)$$

$$\rho = 1 - \frac{P_a}{P} = \frac{EA}{2F_{in} + EA} \quad (9)$$

200 Where r and ρ are the contributions to precipitation from external water vapor
201 transport and local land surface evaporation, respectively, and ρ is the precipitation
202 recirculation rate.

203 The Brubaker binary model water vapor transport process is based mainly on
204 advection terms, which can be applied to calculate the precipitation recirculation rates
205 in the study area. Give that the calculation of these precipitation recirculation rates
206 depends on the size of the selected area, the study area was enlarged (42.5–52.5°
207 N, 115–125° E) for the purpose of calculation.

208 **3. Results**

209 **3.1 scPDSI reconstruction**

210 All the tree ring chronologies show a high mean sensitivity and standard
211 deviation, typical of trees growing in arid and semi-arid regions, due to the location of
212 the Hailar region. The high inter-series correlation suggests that our tree-ring width
213 chronology reliably captures several standard climate signals. The EPS of the RC
214 chronology passed the test for signal strength (EPS > 0.85) after 1796 (Table 2 and



215 Fig. 3). The tree-ring width series has a significant negative correlation with
216 temperature, a significant positive correlation with precipitation, and a significant
217 positive correlation with scPDSI, according to the climate response results ($p < 0.05$)
218 (Fig. 4a, b). Screening for seasonal combinations of temperature, precipitation, and
219 scPDSI revealed the strongest correlation between the RC tree ring width chronology
220 and meant scPDSI from May to July ($r = 0.645$, $p < 0.01$). Accordingly, we
221 reconstructed the May to July scPDSI for the Hailar region since 1796 CE, using the
222 following equation (Fig. 4d):

$$Y = 3.681X - 4.146 \quad (10)$$

$$(n = 70, r = 0.645, R^2 = 41.6\%, R_{adj}^2 = 40.7\%, F = 48.385, p < 0.01)$$

223 Where Y is the mean reconstructed scPDSI for May to July, and X is the tree ring
224 width index from the composite chronology.

225 In equation (10), the correlation between the mean May–July scPDSI and the
226 tree-ring width index over the period of 1951–2020 is 0.645, with the tree-ring width
227 index explaining 41.6% (40.7% after adjustment for the degrees of freedom) of the
228 mean scPDSI variance, $F = 48.385$ and $p < 0.01$. Except for several anomalously high
229 values, the reconstructed mean scPDSI values agree well with the instrumental data
230 (Fig. 4c). The split calibration-verification test results show that the reconstruction
231 model has good reliability and stability, with values of RE and CE > 0.20 . The sign
232 and first-order difference sign tests are significant at the 0.05 level (Table 3). These
233 results suggest that our scPDSI reconstruction has reliably recorded climate signals at
234 low frequencies.



235 **3.2 Characteristics of the scPDSI reconstruction**

236 Our scPDSI reconstructions reveal oscillations between drier and wetter conditions
237 in the Hailar region during 1796–2020 CE (Fig. 4e). Dry/wet periods after 15-year
238 low-pass filtering were continuously below/above the long-term mean for more than
239 10 years. Four dry periods (1809–1819, 1829–1878, 1937–1950, 1990–2012), and
240 five wet periods (1796–1808, 1879–1900, 1910–1936, 1951–1963, 1970–1989) are
241 evident in the record. A data value < 1.5 times the standard deviation of the long-term
242 mean is defined as an extreme drought year, and such years occurred in 1779, 1826,
243 1837, 1840, 1842, 1857, 1864, 1866, 1951, 1996 and 2007. The curves also show an
244 increase following lower values in the 1870s, and a clear decreasing trend in the last
245 10 years, which is consistent with the instrumental observations (Fig. 4e). The results
246 of the MTM analysis revealed periodicities of 2–8.1 years (Fig. 5). The results of
247 spatial correlation analysis revealed a strong positive correlation between the
248 reconstructed scPDSI series on the scale of the upper basin of the Heilongjiang (Amur)
249 River and the gridded scPDSI, total rainfall, and runoff, from May to July (Fig. 6a, b).
250 After obtaining the mean series of the gridded data, good correlations were obtained
251 between the reconstructed scPDSI and the regional mean of the gridded data, with $r =$
252 0.57 ($p < 0.01$), and $r = 0.35$ ($p < 0.01$), with CRU scPDSI and CRU precipitation,
253 respectively (Fig. 6a, b, c). The correlations between reconstructed scPDSI and
254 G-RUN runoff and runoff from the Khabarovsk Hydrological Station runoff were $r =$
255 0.34 ($p < 0.01$) and $r = 0.36$ ($p < 0.01$), respectively (Fig. 6d). These results indicate
256 that our scPDSI reconstructions reliably reflect the regional drought characteristics



257 and changes in runoff in the Upper Heilongjiang (Amur) River Basin.

258 **4. Discussion**

259 **4.1 Climate–tree ring growth relationships and temporal variations** 260 **in regional drought**

261 The positive correlation between tree-ring width and rainfall and the negative
262 correlation with temperature indicate that the increase in the circumference of *Pinus*
263 *sylvestris* var. *Mongolica* in the Hailar area is described by a humidity-sensitive
264 growth model. Temperature is much a greater stressor for tree growth in arid and
265 semi-arid regions than precipitation (Bao et al. 2015; Fang et al. 2010; Sun et al.
266 2012). The higher correlation coefficients between temperature and the tree-ring
267 indices in our dataset indicate that the radial expansion of *P. sylvestris* var.
268 *Mongolica* in the Hailar region is mainly influenced by soil moisture conditions
269 modulated by temperature variations (Fig. 4a). Compared with precipitation alone,
270 PDSI better reflects changes in soil moisture caused by precipitation and temperature
271 stress on the radial growth of trees. The PDSI during the growing season from May to
272 July also shows the highest correlation with scPDSI ($r = 0.645$, $p < 0.01$) (Fig. 4c).
273 The radial growth of *P. sylvestris* var. *Mongolica* is mainly determined by the control
274 of soil moisture by precipitation (Song et al. 2015). However, in semiarid areas, the
275 increasing temperature during the growing season accelerates the evaporation of soil
276 moisture and enhances plant transpiration, and thus the soil moisture supply is
277 insufficient for tree growth (Shang et al. 2012). In contrast, temperatures above a
278 certain threshold during the growth season can adversely affect tree growth because



279 the decrease in the net photosynthetic rate and excessive temperatures will lead to
280 more severe drought stress (D'arrigo et al. 2004).

281 The reconstructed scPDSI reveals ten extreme drought years during 1796–2000,
282 seven of which can be identified in historical documents (Zhang, 2004; Liu and Wen,
283 2008). (Table 4). The historical literature includes detailed descriptions of drought
284 events; for example, 1951 was a drought year throughout Inner Mongolia—one of a
285 series of relatively severe droughts—when the lack of rainfall in summer and autumn
286 was more severe than in spring. Numerous seedlings of crop plants in Hulunbuir were
287 killed by the drought and the grain yield of the entire region was significantly reduced
288 (Liu and Wen, 2008). In 1996, a severe drought affected the north-central part of Inner
289 Mongolia in early summer (Liu and Wen, 2008). Our reconstruction captures several
290 extreme drought events in the past decade. The intense heat in NEC during
291 July–August 2016 resulted in severe crop yield reductions and economic losses
292 amounting to \$15,61 billion (Li et al. 2018). In 2017, NEC experienced the most
293 severe spring and summer drought event of the last few decades (Zeng et al. 2019),
294 which heavily affected the cultivated area in eastern Inner Mongolia, the magnitude of
295 the crop failure and direct economic losses were the second highest since 2012, with
296 the area of 74.3×10^4 km² being affected by drought across the region, and with
297 moderately intense drought occurring mainly in western Hulunbuir (Zhang et al.
298 2017). NEC is a major food-producing region in China, and thus it is of both regional
299 and national importance to improve our understanding of the causes and patterns of
300 drought events and to develop appropriate responses.



301 **4.2 Synoptic meteorological analysis of severe drought**

302 To explore the climatic drivers of the extreme drought events, we screened the
303 wettest and driest decades from 1891 to 2020. SST changes in the previous winter are
304 critical for precipitation in East Asia in the following year (Juneng and Tangang,
305 2005), and thus we selected the winter SST from December of the previous year to
306 January of the current year to analyze the respective decadal SST anomalies. The
307 results indicate that during wet years, SST has the negative ENSO phase pattern,
308 while in dry years, it has the positive ENSO phase pattern (Fig. 7a, b). The
309 reconstructed scPDSI also has the same 2–5 year cycle as ENSO (Fig. 5), suggesting
310 that ENSO may have contributed to drought in the Upper Heilongjiang (Amur) River
311 Basin. The wettest decade and the driest decade from 1950 to 2020 were also selected
312 for climatological analysis, which revealed the following relationships. During the
313 wet years, the SST in the preceding winter had the negative ENSO phase pattern, the
314 SST in the eastern equatorial Pacific decreased, and the western Pacific warm pool
315 and the Walker circulation intensified. At the same time, the western Pacific
316 subtropical high pressure weakened and shifted northward, the Mongolian high
317 pressure weakened significantly (Fig. 8a), the anomalous cyclone in the wet years
318 corresponded to a cold anomaly (Fig. 8c), and the major rainfall band in May–July
319 (MJJ) shifted northward. This scenario caused an anomalous increase in precipitation
320 in the Upper Heilongjiang (Amur) River Basin during the selected wet years. In dry
321 years, the SST in the preceding winter had an ENSO positive phase pattern, the SST
322 difference between the western and eastern equatorial Pacific decreased, the



323 latitudinal Walker circulation weakened, the western Pacific subtropical high pressure
324 strengthens and shifted southward compared to normal. These events result in weak
325 East Asian summer winds and a significantly more intense Mongolian high (Fig. 8b).
326 The anomalous cyclone in dry years corresponds to a warm anomaly (Fig. 8d), and
327 the anticyclone corresponds to a warm anomaly (Fig. 8d), which is controlled by an
328 eccentric northerly component that favors cold air transport from high latitudes to the
329 northeast during dry years. This results in anomalous descending motion and a
330 southward shift of the main rain and wind belts, leading to drought (Fig. 8f).

331 The geopotential height distance level field results show a similar pattern to that of
332 the Silk Road remote correlation model (Enomoto et al. 2003), which is strongly
333 correlated with precipitation in East Asia. The distribution of drought and
334 precipitation anomalies analyzed by the Silk Road remote correlation model is
335 consistent, suggesting that the summer drought in NEC in summer is strongly related
336 to the precipitation deficit. At the same time, ENSO may intensify the reduced
337 precipitation in NEC via its influence on the Indian summer winds, as indicated by the
338 Silk Road remote correlation model (Dai, 2011; Wu et al. 2003). In summary, the
339 large-scale ocean-atmosphere-land circulation system is a critical driver of drought
340 development in the Upper Heilongjiang (Amur) River Basin.

341 **4.3 Atmospheric water cycle during drought years**

342 Based on NCEP-NCAR reanalysis 1 data (Kalnay et al. 1996), we quantified the
343 meteorological conditions and atmospheric hydrological cycle anomalies in the Hailar
344 region during May–July of the driest decade of 1950–2020, based on the



345 reconstructed scPDSI. The total climatic precipitation for May–July of 1950–2020
346 was 27.0×10^6 kg/s, while the total precipitation for May–July in a drought year was
347 23.0×10^6 kg/s, a decrease of 14.8%. The external advective input (F_{in}) under
348 climatic conditions was 230.9×10^6 kg/s, compared to 211.4×10^6 kg/s during the dry
349 year, with an 8.4% reduction in external advective input during the drought.
350 Evaporation (E) was 30.7×10^6 kg/s under these climatic conditions, and 29.5×10^6
351 kg/s during dry years, with a 3.9% reduction in evaporation during the drought.
352 Precipitation formed by external advective input (P_a) under these climatic conditions
353 was 25.3×10^6 kg/s, contributing 93.8% to precipitation, and precipitation formed by
354 evaporation (P_e) was 1.7×10^6 kg/s, with a precipitation recirculation rate of 6.2%.
355 Precipitation formed by external advection input (P_a) during the dry year was $21.4 \times$
356 10^6 kg/s, contributing 93.5% to precipitation, and precipitation formed by evaporation
357 (P_e) was 1.5×10^6 kg/s, with the precipitation recirculation rate of 6.5% (Fig. 9b).
358 During the dry year, total precipitation decreased by 14.8% compared to the climatic
359 mean, and the external advective input of water vapor decreased significantly (8.4%),
360 resulting in a 15.4% decrease in precipitation formed from the external advective
361 input of water vapor, with little change in evaporation and precipitation formed by
362 evaporation. These results suggest that the drought in the Upper Heilongjiang (Amur)
363 Basin is mainly caused by a reduction in the external advective water vapor input
364 rather than by anomalies in the precipitation cycle. Synthetic anomalies in the whole
365 layer water vapor fluxes and precipitation rates also indicate a decrease in advective
366 water vapor transport and precipitation during the drought (Fig. 9a). These results



367 suggest that water vapor transport processes play a key role in the development of
368 drought in the Upper Heilongjiang (Amur) River Basin.

369 **5. Conclusion**

370 We built a composite tree-ring chronology for two sampling sites in the Hailar
371 region. Based on this chronology, we reconstructed the monthly mean scPDSI for
372 May–July in the Upper Heilongjiang (Amur) Basin since 1796. the reconstructed
373 sequence comprises more than 220 years of wet and dry variations in the Upper
374 Heilongjiang (Amur) River Basin, which experienced four consecutive dry periods
375 and five consecutive wet periods, since 1796 CE, with a significant 2-8-year
376 cyclicity. The drought reconstruction accurately captured the recent trends in dry/wet
377 variability and it reflects drought variability across a large area.

378 Our synoptic climatological analysis of extreme drought years suggests that the
379 dry/wet variability in the Upper Heilongjiang (Amur) River Basin is related to several
380 large-scale climate stresses and atmospheric circulation patterns (the ENSO and Silk
381 Road models), and that one of the critical drivers of drought development in the
382 Upper Heilongjiang (Amur) River Basin is the large-scale ocean-atmosphere-land
383 circulation system. Our atmospheric water circulation analysis suggests that the cause
384 of drought is primarily a reduction in advective water vapor transport, rather than
385 precipitation circulation processes, which further implies that atmospheric circulation
386 systems control wet/dry variability in the Upper Heilongjiang (Amur) River Basin.

387 Our drought reconstruction has several shortcomings since it is based on only two
388 sample sites, and it spans a relatively short interval (230 years), and represents only a



389 very small region. Therefore, it is essential to systematically compile additional tree
390 ring-based climate records from this region to provide drought reconstructions on a
391 large spatial scale, which may help characterize the spatio-temporal variability and
392 impact mechanisms of drought within NEC.

393 **6. Code and data availability**

394 ScPDSI reconstruction in the Upper Heilongjiang (Amur) River Basin will be
395 available in the Supplement. The data that support the findings of this study are
396 available from the corresponding author upon reasonable request.

397 **7. Author contribution**

398 Feng Chen conceived the study, Yang Xu conducted the analyses and wrote the
399 manuscript, other authors were involved in the sample collection. All authors
400 interpreted and discussed the results.

401 **8. Acknowledgements**

402 This research was supported by the National Natural Science Foundation of China
403 (32061123008).

404 **9. References**

- 405 Bao, G., Liu, Y., Liu, N., and Linderholm, H. W.: Drought variability in eastern Mongolian Plateau and
406 its linkages to the large-scale climate forcing, *Climate Dynamics*, 44, 717-733, <https://doi.org/10.1007/s00382-014-2273-7>, 2015.
- 408 Brubaker, K. L., Entekhabi, D., and Eagleson, P. S.: ESTIMATION OF CONTINENTAL
409 PRECIPITATION RECYCLING, *Journal of Climate*, 6, 1077-1089,
410 [https://doi.org/10.1175/1520-0442\(1993\)006<1077:Eocpr>2.0.Co;2](https://doi.org/10.1175/1520-0442(1993)006<1077:Eocpr>2.0.Co;2), 1993.
- 411 Burde, G. I. and Zangvil, A.: The estimation of regional precipitation recycling. Part I: Review of
412 recycling models, *Journal of Climate*, 14, 2497-2508, <https://doi.org/10.1175/1520->



- 413 0442(2001)014
414 <2497:Teorpr>2.0.Co;2, 2001.
- 415 Chen, F., Opala-Owczarek, M., Khan, A., Zhang, H. L., Owczarek, P., Chen, Y. P., Ahmed, M., and
416 Chen, F.: Late twentieth century rapid increase in high Asian seasonal snow and glacier-derived
417 streamflow tracked by tree rings of the upper Indus River basin, *Environmental Research Letters*,
418 16, <https://doi.org/10.1088/1748-9326/ac1b5c>, 2021.
- 419 Chen, F., Martin, H., Zhao, X., Roig, F., Zhang, H. L., Wang, S. J., Yue, W. P., and Chen, Y. P.:
420 Abnormally low precipitation-induced ecological imbalance contributed to the fall of the Ming
421 Dynasty: new evidence from tree rings, *Climatic Change*, 173,
422 <https://doi.org/10.1007/s10584-022-03406-y>, 2022.
- 423 Chen, Z. J., Zhang, X. L., Cui, M. X., He, X. Y., Ding, W. H., and Peng, J. J.: Tree-ring based
424 precipitation reconstruction for the forest-steppe ecotone in northern Inner Mongolia, China and
425 its linkages to the Pacific Ocean variability, *Global and Planetary Change*, 86-87, 45-56,
426 [https://doi.org/10.1016/](https://doi.org/10.1016/j.gloplacha.2012.01.009)
427 [j.gloplacha.2012.01.009](https://doi.org/10.1016/j.gloplacha.2012.01.009), 2012.
- 428 Cook, B. I., Anchukaitis, K. J., Touchan, R., Meko, D. M., and Cook, E. R.: Spatiotemporal drought
429 variability in the Mediterranean over the last 900years, *Journal of Geophysical*
430 *Research-Atmospheres*, 121, 2060-2074, <https://doi.org/10.1002/2015jd023929>, 2016.
- 431 Cook, E. R.: A time series analysis approach to tree ring standardization, University of Arizona Tucson,
432 1985.
- 433 Cook, E. R. and Kairiukstis, L. A.: *Methods of dendrochronology: applications in the environmental*
434 *sciences*, Springer Science & Business Media, 2013.
- 435 Cook, E. R., Anchukaitis, K. J., Buckley, B. M., D'Arrigo, R. D., Jacoby, G. C., and Wright, W. E.:
436 Asian Monsoon Failure and Megadrought During the Last Millennium, *Science*, 328, 486-489,
437 <https://doi.org/10.1126/science.1185188>, 2010.
- 438 D'Arrigo, R. D., Kaufmann, R. K., Davi, N., Jacoby, G. C., Laskowski, C., Myneni, R. B., and
439 Cherubini, P.: Thresholds for warming-induced growth decline at elevational tree line in the Yukon
440 Territory, Canada, *Global Biogeochemical Cycles*, 18, <https://doi.org/10.1029/2004gb002249>,
441 2004.
- 442 Dai, A. G.: Drought under global warming: a review, *Wiley Interdisciplinary Reviews-Climate Change*,



- 443 2, 45-65, <https://doi.org/10.1002/wcc.81>, 2011.
- 444 Ding, Y. H., Sun, Y., Wang, Z. Y., Zhu, Y. X., and Song, Y. F.: Inter-decadal variation of the summer
445 precipitation in China and its association with decreasing Asian summer monsoon Part II: Possible
446 causes, *International Journal of Climatology*, 29, 1926-1944, <https://doi.org/10.1002/joc.1759>,
447 2009.
- 448 Enomoto, T., Hoskins, B. J., and Matsuda, Y.: The formation mechanism of the Bonin high in August,
449 *Quarterly Journal of the Royal Meteorological Society*, 129, 157-178, <https://doi.org/10.1256/qj>.
450 01.211, 2003.
- 451 Fang, K. Y., Gou, X. H., Chen, F. H., D'Arrigo, R., and Li, J. B.: Tree-ring based drought reconstruction
452 for the Guiqing Mountain (China): linkages to the Indian and Pacific Oceans, *International Journal*
453 *of Climatology*, 30, 1137-1145, <https://doi.org/10.1002/joc.1974>, 2010.
- 454 Findell, K. L. and Eltahir, E. A. B.: Atmospheric controls on soil moisture-boundary layer interactions.
455 Part I: Framework development, *Journal of Hydrometeorology*, 4, 552-569,
456 [https://doi.org/10.1175/1525-7541\(2003\)004<0552:Acosml>2.0.Co;2](https://doi.org/10.1175/1525-7541(2003)004<0552:Acosml>2.0.Co;2), 2003.
- 457 Fritts, H. C.: *Reconstructing large-scale climatic patterns from tree-ring data: a diagnostic analysis*,
458 University of Arizona Press 1991.
- 459 Fu, C. B. and Zeng, Z. M.: Correlations between North Atlantic Oscillation Index in winter and eastern
460 China Flood/Drought Index in summer in the last 530 years, *Chinese Science Bulletin*, 50,
461 <https://doi.org/2505-2516>, 10.1360/04wd0284, 2005.
- 462 Ghiggi, G., Humphrey, V., Seneviratne, S. I., and Gudmundsson, L.: G-RUN ENSEMBLE: A
463 Multi-Forcing Observation-Based Global Runoff Reanalysis, *Water Resources Research*, 57,
464 2021.
- 465 Guan, Y. S., Gu, X. H., Slater, L. J., Li, L. F., Kong, D. D., Liu, J. Y., Zhang, X., and Yan, X. S.:
466 Tracing anomalies in moisture recycling and transport to two record-breaking droughts over the
467 Mid-to-Lower Reaches of the Yangtze River, *Journal of Hydrology*, 609, [https://doi.org/10.1016/](https://doi.org/10.1016/j.jhydrol)
468 [j.jhydrol](https://doi.org/10.1016/j.jhydrol).
469 2022.127787, 2022.
- 470 Guo, L., Klingaman, N. P., Demory, M. E., Vidale, P. L., Turner, A. G., and Stephan, C. C.: The
471 contributions of local and remote atmospheric moisture fluxes to East Asian precipitation and its
472 variability, *Climate Dynamics*, 51, 4139-4156, <https://doi.org/10.1007/s00382-017-4064-4>, 2018.



- 473 Han, T. T., Chen, H. P., and Wang, H. J.: Recent changes in summer precipitation in Northeast China
474 and the background circulation, *International Journal of Climatology*, 35, 4210-4219,
475 <https://doi.org/10.1002/joc.4280>, 2015.
- 477 Han, T. T., Wang, H. J., and Sun, J. Q.: Strengthened Relationship between Eastern ENSO and Summer
478 Precipitation over Northeastern China, *Journal of Climate*, 30, 4497-4512, <https://doi.org/10.1175/jcli-d-16-0551.1>, 2017.
- 480 Harris, I., Jones, P. D., Osborn, T. J., and Lister, D. H.: Updated high-resolution grids of monthly
481 climatic observations - the CRU TS3.10 Dataset, *International Journal of Climatology*, 34,
482 623-642, <https://doi.org/10.1002/joc.3711>, 2014.
- 483 Holmes, R. L.: Computer-assisted quality control in tree-ring dating and measurement, 1983.
- 484 Juneng, L. and Tangang, F. T.: Evolution of ENSO-related rainfall anomalies in Southeast Asia region
485 and its relationship with atmosphere-ocean variations in Indo-Pacific sector, *Climate Dynamics*,
486 25, 337-350, <https://doi.org/10.1007/s00382-005-0031-6>, 2005.
- 487 Kalnay, E., Kanamitsu, M., Kistler, R., Collins, W., Deaven, D., Gandin, L., Iredell, M., Saha, S., White,
488 G., Woollen, J., Zhu, Y., Chelliah, M., Ebisuzaki, W., Higgins, W., Janowiak, J., Mo, K. C.,
489 Ropelewski, C., Wang, J., Leetmaa, A., Reynolds, R., Jenne, R., and Joseph, D.: The
490 NCEP/NCAR 40-year reanalysis project, *Bulletin of the American Meteorological Society*, 77,
491 437-471, [https://doi.org/10.1175/1520-0477\(1996\)077<0437:Tnyrp>2.0.Co;2](https://doi.org/10.1175/1520-0477(1996)077<0437:Tnyrp>2.0.Co;2), 1996.
- 492 Lesk, C., Rowhani, P., and Ramankutty, N.: Influence of extreme weather disasters on global crop
493 production, *Nature*, 529, 84-+, <https://doi.org/10.1038/nature16467>, 2016.
- 494 Li, H., Chen, H., Wang, H., Sun, J., and Ma, J.: Can Barents Sea ice decline in spring enhance summer
495 hot drought events over northeastern China?, *Journal of Climate*, 31, 4705-4725, 2018.
- 496 Li, Y., Zhang, L., and Wang, B.: Contributions of Local and Remote Water Vapor Transport to
497 Precipitation Variations over Songhua River Basin, *Chinese Journal of Atmospheric Sciences*, 44,
498 611-624, 2020.
- 499 Li, Y. H., Yuan, X., Zhang, H. S., Wang, R. Y., Wang, C. H., Meng, X. H., Zhang, Z. Q., Wang, S. S.,
500 Yang, Y., Han, B., Zhang, K., Wang, X. P., Zhao, H., Zhou, G. S., Zhang, Q., He, Q., Guo, N., Hou,
501 W., Zhang, C. J., Xiao, G. J., Sun, X. Y., Yue, P., Sha, S., Wang, H. L., Zhang, T. J., Wang, J. S.,
502 and Yao, Y. B.: Mechanisms and Early Warning of Drought Disasters: Experimental Drought



- 503 Meteorology Research over China, *Bulletin of the American Meteorological Society*, 100,
504 673-687, <https://doi.org/10.1175/bams-d-17-0029.1>, 2019.
- 505 Liang, E. Y., Shao, X. M., Liu, H. Y., and Dieter, E.: Tree-ring based PDSI reconstruction since AD
506 1842 in the ortindag sand land, east inner mongolia, *Chinese Science Bulletin*, 52, 2715-2721,
507 <https://doi.org/10.1007/s11434-007-0351-5>, 2007.
- 508 Liu, G. and Wen, K.: *Chinese Meteorological Disasters Ceremony (Inner Mongolia Volume)*, 2008.
- 509 Liu, N., Liu, Y., Bao, G., Bao, M., Wang, Y. C., Zhang, L. Z., Ge, Y. X., Bao, W., and Tian, H.: Drought
510 reconstruction in eastern Hulun Buir steppe, China and its linkages to the sea surface temperatures
511 in the Pacific Ocean, *Journal of Asian Earth Sciences*, 115, 298-307, [https://doi.org/10.1016/](https://doi.org/10.1016/j.jseas.2015.10.009)
512 [j.jseas.](https://doi.org/10.1016/j.jseas.2015.10.009)
513 2015.10.009, 2016.
- 514 Liu, Y., Bao, G., Song, H. M., Cai, Q. F., and Sun, J. Y.: Precipitation reconstruction from Hailar pine
515 (*Pinus sylvestris* var. *mongolica*) tree rings in the Hailar region, Inner Mongolia, China back to
516 1865 AD, *Palaeogeography Palaeoclimatology Palaeoecology*, 282, 81-87, [https://doi.org/10.1016/](https://doi.org/10.1016/j.palaeo.2009.08.012)
517 [j.palaeo.2009.08.012](https://doi.org/10.1016/j.palaeo.2009.08.012), 2009.
- 518 Mann, M. E. and Lees, J. M.: Robust estimation of background noise and signal detection in climatic
519 time series, *Climatic change*, 33, 409-445, 1996.
- 520 Pearson, C., Salzer, M., Wacker, L., Brewer, P., Sookdeo, A., and Kuniholm, P.: Securing timelines in
521 the ancient Mediterranean using multiproxy annual tree-ring data (vol 117, pg 8410, 2020),
522 *Proceedings of the National Academy of Sciences of the United States of America*, 117,
523 18891-18891, <https://doi.org/10.1073/pnas.2013168117>, 2020.
- 524 Schubert, S. D., Wang, H. L., Koster, R. D., Suarez, M. J., and Groisman, P. Y.: Northern Eurasian Heat
525 Waves and Droughts, *Journal of Climate*, 27, 3169-3207, <https://doi.org/10.1175/jcli-d-13-00360.1>,
526 2014.
- 527 Shang, J., Shi, Z., Gao, J., Xu, L., Lu, S., Feng, C., and Wang, L.: Response of tree-ring width of *Pinus*
528 *syvestris* var. *mongolica* to climate change in Hulunbuir sand land, China, *Acta Ecologica Sinica*,
529 32, 1077-1084, 2012.
- 530 Song, L., Liu, B., Zhang, H., and Liu, Y.: Response of *Pinus sylvestris* var. *mongolica* Tree-ring Width
531 to Climate Change in Hulunbuir Sandy Land, China, *Journal of North-East Forestry University*, 43,
532 17, 2015.



- 533 Sun, J. Y., Liu, Y., Sun, B., and Wang, R. Y.: Tree-ring based PDSI reconstruction since 1853 AD in the
534 source of the Fenhe river basin, Shanxi province, China, *Science China-Earth Sciences*, 55,
535 1847-1854, <https://doi.org/10.1007/s11430-012-4369-4>, 2012.
- 536 Trenberth, K. E., Dai, A. G., van der Schrier, G., Jones, P. D., Barichivich, J., Briffa, K. R., and
537 Sheffield, J.: Global warming and changes in drought, *Nature Climate Change*, 4, 17-22,
538 <https://doi.org/10.1038/nclimate2067>, 2014.
- 540 Wang, H. J.: The instability of the East Asian summer monsoon - ENSO relations, *Advances in*
541 *Atmospheric Sciences*, 19, 1-11, 2002.
- 542 Wang, H. J. and He, S. P.: The North China/Northeastern Asia Severe Summer Drought in 2014,
543 *Journal of Climate*, 28, 6667-6681, <https://doi.org/10.1175/jcli-d-15-0202.1>, 2015.
- 544 Wang, L. Y., Yuan, X., Xie, Z. H., Wu, P. L., and Li, Y. H.: Increasing flash droughts over China during
545 the recent global warming hiatus, *Scientific Reports*, 6, <https://doi.org/10.1038/srep30571>, 2016.
- 546 Wang, S. S., Yuan, X., and Li, Y. H.: Does a Strong El Nino Imply a Higher Predictability of Extreme
547 Drought?, *Scientific Reports*, 7, <https://doi.org/10.1038/srep40741>, 2017.
- 548 Wang, X., Zhang, C., Hasi, E., and Dong, Z.: Has the Three Norths Forest Shelterbelt Program solved
549 the desertification and dust storm problems in arid and semiarid China?, *Journal of Arid*
550 *Environments*, 74, 13-22, 2010.
- 551 Wu, R. G., Hu, Z. Z., and Kirtman, B. P.: Evolution of ENSO-related rainfall anomalies in East Asia,
552 *Journal of Climate*, 16, 3742-3758,
553 [https://doi.org/10.1175/1520-0442\(2003\)016<3742:EOerai>2.0.](https://doi.org/10.1175/1520-0442(2003)016<3742:EOerai>2.0.CO;2)
554 [Co;2](https://doi.org/10.1175/1520-0442(2003)016<3742:EOerai>2.0.CO;2), 2003.
- 555 Xu, Z. Q., Fan, K., and Wang, H. J.: Role of sea surface temperature anomalies in the tropical
556 Indo-Pacific region in the northeast Asia severe drought in summer 2014: month-to-month
557 perspective, *Climate Dynamics*, 49, 1631-1650, <https://doi.org/10.1007/s00382-016-3406-y>, 2017.
- 558 Yu, R. C., Wang, B., and Zhou, T. J.: Tropospheric cooling and summer monsoon weakening trend over
559 East Asia, *Geophysical Research Letters*, 31, <https://doi.org/10.1029/2004gl021270>, 2004.
- 560 Yuan, X. and Wood, E. F.: Multimodel seasonal forecasting of global drought onset, *Geophysical*
561 *Research Letters*, 40, 4900-4905, <https://doi.org/10.1002/grl.50949>, 2013.
- 562 Zeng, D. W., Yuan, X., and Roundy, J. K.: Effect of Teleconnected Land-Atmosphere Coupling on



563 Northeast China Persistent Drought in Spring-Summer of 2017, *Journal of Climate*, 32, 7403-7420,
564 <https://doi.org/10.1175/jcli-d-19-0175.1>, 2019.

565 Zhang, D. e.: A compendium of Chinese meteorological records of the last 3000 years, Jiangsu
566 Education House, Nanjing, 2004.

567 Zhang, G. L., Xu, X. L., Zhou, C. P., Zhang, H. B., and Ouyang, H.: Responses of grassland vegetation
568 to climatic variations on different temporal scales in Hulun Buir Grassland in the past 30 years,
569 *Journal of Geographical Sciences*, 21, 634-650, <https://doi.org/10.1007/s11442-011-0869-y>, 2011.

570 Zhang, L., Fang, X., Ren, G., and Suo, X.: Environmental changes in the North China farming-grazing
571 transitional zone, *Earth Science Frontiers*, 4, 127-134, 1997.

572 Zhang, Y., Zhang, L., Wang, S., and Feng, J.: Drought events and their influence in summer of 2017 in
573 China, *J. Arid Meteor*, 35, 899-905, 2017.

574 Zhao, Y. and Zhou, T. J.: Interannual Variability of Precipitation Recycle Ratio Over the Tibetan
575 Plateau, *Journal of Geophysical Research-Atmospheres*, 126,
576 <https://doi.org/10.1029/2020jd033733>, 2021.

577

578

579

580

581

582

583

584

585

586

587

588



589 **Table**

590

591 **Table 1.** Information about the tree-ring sampling sites in the Upper Amur
 592 (Heilongjiang) River Basin.

593

Site code	Lat. (N)	long. (E)	Elevation (m)	Sample	Species
MGET	121°49'	46°42'	1120	63/33	<i>Pinus sylvestris</i>
NEGC	118°44'	49°12'	1540	40/20	<i>Pinus sylvestris</i>
RC				103/53	<i>Pinus sylvestris</i>

594

595 **Table 2.** Statistical properties of the tree-ring width chronologies from the Upper
 596 Amur (Heilongjiang) River Bas

Statistic	MGET	NEGC	RC
Mean sensitivity	0.285	0.367	0.307
Standard deviation	0.198	0.21	0.19
Mean correlation between the trees	0.658	0.723	0.653
Signal to noise ratio (SNR)	86.651	60.15	26.063
Variance of the first eigenvector (%)	58.6	66.4	38.6
First year when EPS > 0.85 (tree number)	1762(5)	1900(4)	1796(10)

597

598 **Table 3.** Results of verification and calibration tests for the scPDSI reconstruction.

Statistical procedure	Calibration (1951-1985)	Verification (1986-2020)	Calibration (1986-2020)	Verification (1951-1985)	Full calibration (1951-2020)
R	0.727	0.611	0.661	0.611	0.645
r ²	0.529	0.374	0.436	0.374	0.416
RE		0.357		0.491	
CE		0.378		0.566	
Sign test		24+/11-		23+/12-	
First-order sign test		22+/12-		22+/12-	

599

600

601

602

603



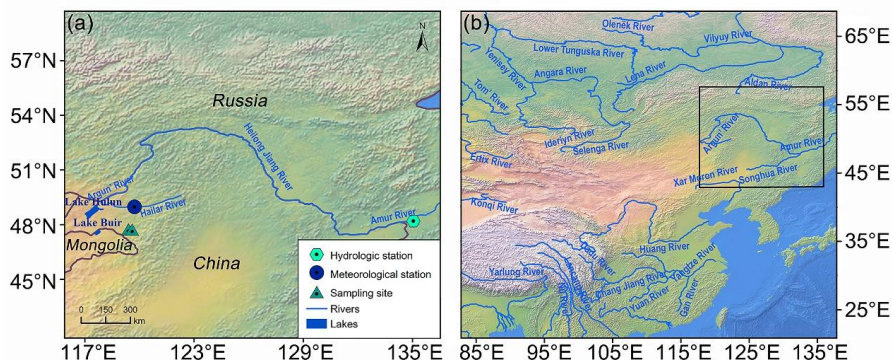
604

605 **Table 4.** Comparisons between the reconstructed scPDSI and documented climatic
 606 events.

Year	PDSI ₅₋₇	Local historical documents
1779	-2.93	Famine in Taiyuan and Baotou
1837	-2.31	Drought in Qiqihaer
1842	-2.62	Drought in Baotou
1857	-2.28	Drought in Baotou and the Qingshuihe river
1866	-2.79	Drought in Hulunbuir
1951	-3.01	Inner Mongolia region drought, decrease I in Hulunbuir grain production
1996	-2.23	Drought in North Central Inner Mongolia in early summer

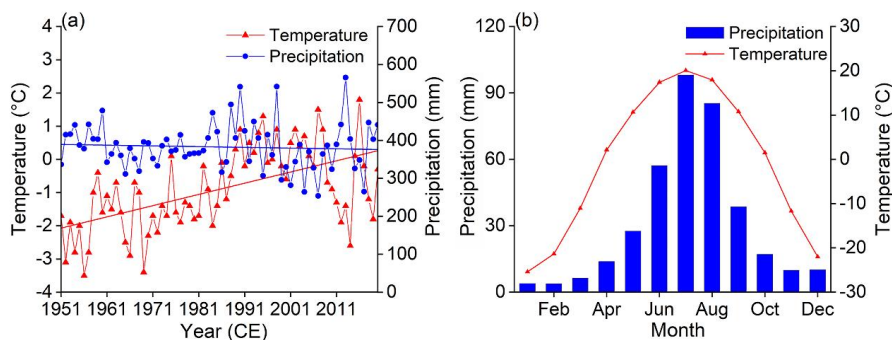
607

608 **Figures**



609

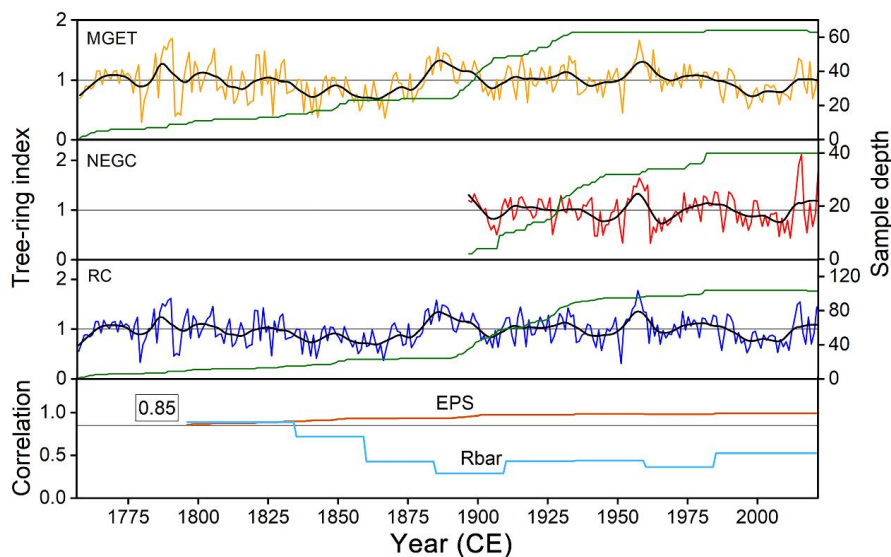
610 **Figure 1.** (a) Location of the tree-ring sampling sites, and meteorological and
 611 hydrological stations in the Upper Amur (Heilongjiang) River Basin. (b) Location of
 612 the study area in Asia. (The raster data for the production of the map was taken from
 613 <https://www.naturalearthdata.com/>)



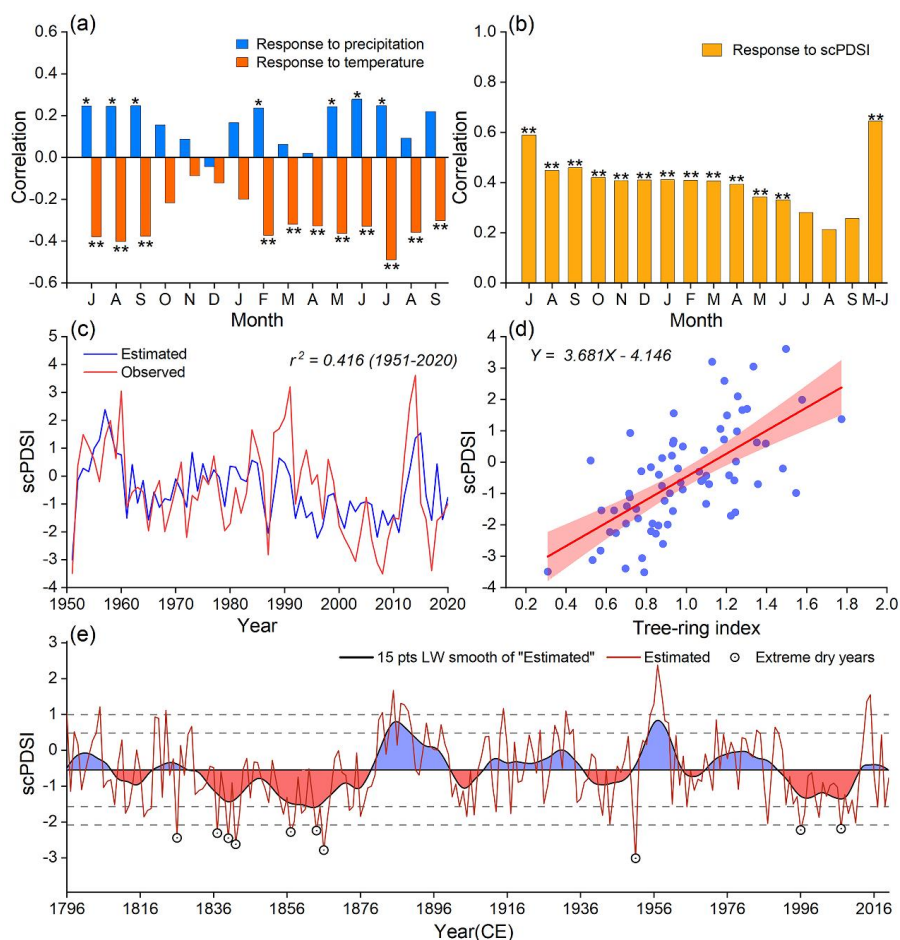
614



615 **Figure 2.** (a) Annual precipitation and temperature trends for the Upper Amur
616 (Heilongjiang) River Basin from 1951 to 2020. (b) Monthly total precipitation and
617 mean temperature for the Upper Amur (Heilongjiang) River Basin.
618



619 **Figure 3.** Chronologies of the two tree-rings records (MGET and NEGC) and the RC
620 from the Upper Amur (Heilongjiang) River Basin. The inter-series correlation (Rbar)
621 and the EPS are shown in the lowermost panel.
622
623



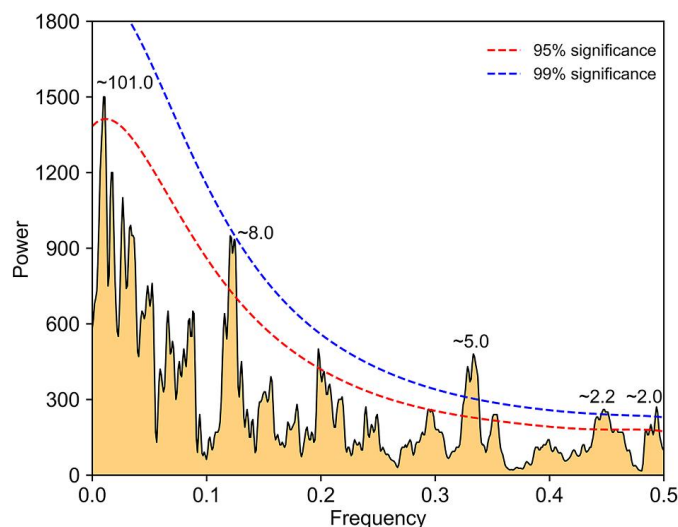
624

625 **Figure 4.** (a) Correlation coefficients between the tree-ring chronologies and monthly
 626 total precipitation and mean temperature. (b) Correlation coefficients between the RC
 627 tree-ring chronologies and monthly mean scPDSI of the CRU. Correlations are
 628 calculated from the previous June to the current September over the time period of
 629 1951–2020 (* represent the 95% significance level, and ** represents the 99%
 630 significance level). (c) Comparison between the instrumental and reconstructed mean
 631 May–July scPDSI for the Hailar region during 1951–2020. (d) One-dimensional
 632 linear regression fits for the May to July scPDSI for 1796–2020. (e) Reconstructed
 633 mean May–July scPDSI and its 15-year low-pass filtered version since 1796 CE. The
 634 horizontal central line represents the average reconstructed scPDSI. The horizontal
 635 dotted lines represent ± 1 SD and ± 1.5 SD on a mean value basis.

636

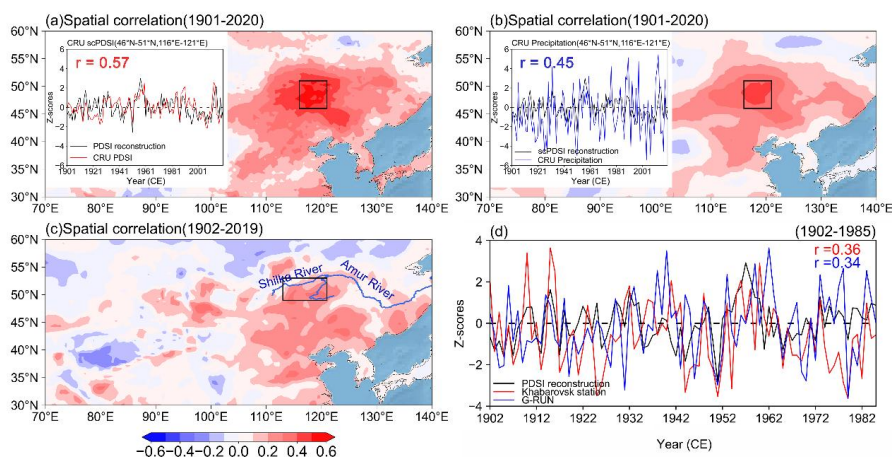
637

638



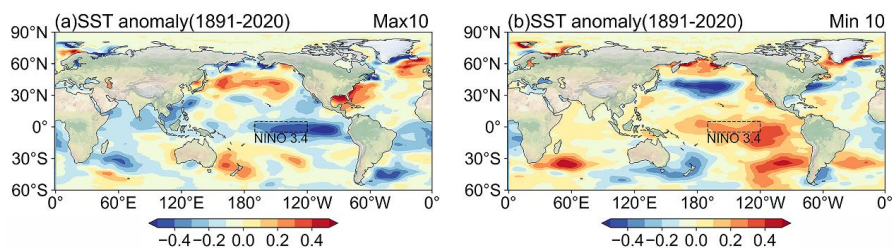
639

640 **Figure 5.** MTM spectral density of the drought reconstruction. The dashed curves
 641 represent the 95% (red) and 99% (blue) significance levels, respectively.



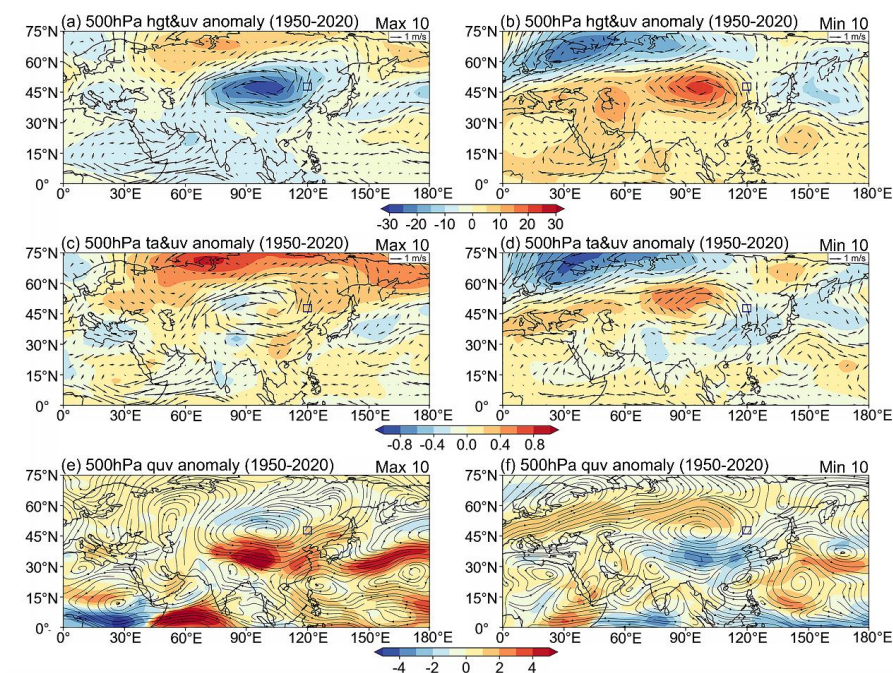
642

643 **Figure 6.** Spatial correlation maps of the reconstructed scPDSI with the CRU gridded
 644 mean May–July scPDSI (a) and the CRU gridded total May–July precipitation (b)
 645 since 1901 CE. The rectangle indicates the location of the range of the grid, and the
 646 same below. The inset graphs show a comparison of the reconstructed scPDSI with
 647 the regional mean scPDSI and precipitation curves from the CRU. (c) Reconstructed
 648 scPDSI with G-RUN gridded May–July mean runoff spatial correlation maps for the
 649 period of 1902–2019. (d) Comparison of reconstructed scPDSI, hydrological station
 650 runoff data, and the G-RUN regional mean runoff data for the period of 1902–1985.



651

652 **Figure 7.** Composite maps of SST anomalies (°C) for the 10 wettest years (a) and 10
653 driest years (b) from the previous December to the current January during 1891–2020.
654



655

656 **Figure 8.** Spatial patterns of geopotential height and 500 hPa vector wind anomalies
657 (a, b), 500 hPa air temperature, and 500 hPa vector wind anomalies (c, d), 500 hPa
658 water vapor transport anomalies (e, f) in the wettest decade and the driest decade
659 during 1950–2020 in NCEP-NCAR Reanalysis 1. The rectangle indicates the location
660 of the study area.

661

662

663

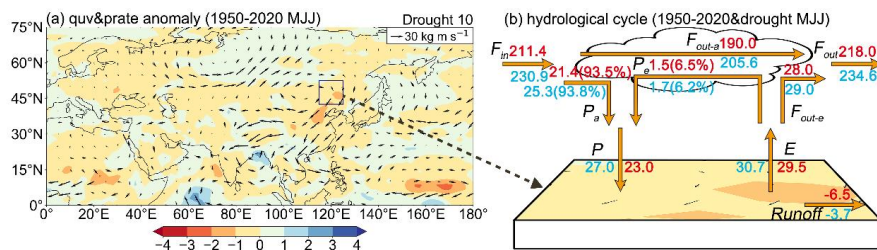
664

665

666



667



668

669 **Figure 9.** (a) Anomaly composites of the mean precipitation rate ($\text{kg/s}\cdot\text{m}^2$) and the
 670 whole layer moisture flux ($\text{kg}\cdot\text{m/s}$) for May–July of the driest decade in the study area
 671 ($115\text{--}125^\circ\text{E}$, $42.5\text{--}52.5^\circ\text{N}$) relative to that of May–July for the period of 1950–2020
 672 (arrows represent the the whole layer moisture flux, filled colors represent the
 673 precipitation rate). (b) Schematic diagram of the land-atmosphere water balance in the
 674 study area during the climatic period (1950–2020) and dry years. The variables in this
 675 plot (i.e., F_{in} , F_{out-a} , F_{out-e} , F_{out-b} , P_a , P_e , P , E) are explained in Section 2.4. The
 676 blue labels (in kg/s) indicate climatic averages, while the red labels indicate averages
 677 during drought.